Neuromorphic learning with Mott insulator NiO

Zhen Zhang[a,1,2], Sandip Mondal[a,1], Subhasish Mandal[b,1], Jason M. Allred[c,1], Neda Alsadat Aghamiri[d], Alireza Fali[d], Zhan Zhang[e], Hua Zhou[e], Hui Cao[f], Fanny Rodolakis[e], Jessica L. McChesney[e], Qi Wang[a], Yifei Sun[a], Yohannes Abate[d], Kaushik Roy[c], Karin M. Rabe[b,2], and Shriram Ramanathan[a,2]

[a]School of Materials Engineering, Purdue University, West Lafayette, IN 47907; [b]Department of Physics and Astronomy, Rutgers University, Piscataway, NJ 08854; [c]School of Electrical and Computer Engineering, Purdue University, West Lafayette, IN 47907; [d]Department of Physics and Astronomy, University of Georgia, Athens, GA 30602; [e]X-Ray Science Division, Advanced Photon Source, Argonne National Laboratory, Lemont, IL 60439; and [f]Materials Science Division, Argonne National Laboratory, Lemont, IL 60439

Contributed by Karin M. Rabe, July 21, 2021 (sent for review August 24, 2020; reviewed by Nicole Benedek and Steven May)

Habituation and sensitization (nonassociative learning) are among the most fundamental forms of learning and memory behavior present in organisms that enable adaptation and learning in dynamic environments. Emulating such features of intelligence found in nature in the solid state can serve as inspiration for algorithmic simulations in artificial neural networks and potential use in neuromorphic computing. Here, we demonstrate nonassociative learning with a prototypical Mott insulator, nickel oxide (NiO), under a variety of external stimuli at and above room temperature. Similar to biological species such as *Aplysia*, habituation and sensitization of NiO possess time-dependent plasticity relying on both strength and time interval between stimuli. A combination of experimental approaches and first-principles calculations reveals that such learning behavior of NiO results from dynamic modulation of its defect and electronic structure. An artificial neural network model inspired by such nonassociative learning is simulated to show advantages for an unsupervised clustering task in accuracy and reducing catastrophic interference, which could help mitigate the stability–plasticity dilemma. Mott insulators can therefore serve as building blocks to examine learning behavior noted in biology and inspire new learning algorithms for artificial intelligence.

neuromorphic learning | Mott insulator | transition metal oxides

Integrating features of artificial intelligence into a vast array of fields from information processing, autonomous systems, and decision and design making to forecasting and healthcare is moving our society toward energy sustainability, high efficiency, and solving complex problems (1–4). A key challenge in neuromorphic computing is the emulation of animal learning with synthetic matter to allow direct implementation of these forms of learning in hardware.

One of the primary forms of learning present in both vertebrate and invertebrate biological species is nonassociative learning (habituation and sensitization), which enables adaptation and learning from the environment (5–8). Nonassociative learning in *Aplysia*, a sea slug that is widely studied as a model system in neuroscience due to strong and easily stimulated behaviors, is schematically shown in Fig. 1 *A* and *B* (8). The gill withdrawal, a form of defensive reflex, is monitored under a weak touch on the siphon. Repeated siphon tactile stimulus results in reducing of gill withdrawal reflex, i.e., habituation. Upon presentation of an electric shock to the tail (new stimulus), sensitization behavior appears where the gill withdrawal response becomes extremely enlarged (9, 10). The neuron potentials monitored from the gill reflex neural circuit (Fig. 1*B*) demonstrate that while the sensory neural potential remains almost identical, a decrement of motor neural potential appears during habituation and a substantial increase of motor neuronal potential emerges upon sensitizing stimulus (11). As a result, habituation appears as a reduction in response due to repeated exposure to a single environmental stimulus, while sensitization manifests as an extreme increment of response by the introduction of a noxious stimulus (6). These learning behaviors were reported to result from a change in the synaptic weight (8).

Emulation of both habituation and sensitization behavior within solid-state systems is still a fledgling field. Materials with highly tunable electronic structures and dynamical response to environmental stimuli are of great interest in this regard (12). Nickel oxide is a prototypical Mott insulator with strong correlation of electrons in Ni 3d orbitals resulting in a charge–transfer gap between the Ni 3d upper Hubbard band and O 2p band (Fig. 1*D*) (13, 14). The sensitivity of the electron correlation effects to charged point defects leads to measurable response to subtle changes in environmental stimuli, such as pressure (15), electric field (16), chemical doping (17), and variation of oxygen partial pressures (18).

In this work, we demonstrate the emulation of biological nonassociative learning with binary nickel oxide under a variety of environmental stimuli by dynamical modulation of their defect and electronic structures. NiO thin-film devices with Pt electrodes were exposed to hydrogen and ozone gas (Fig. 1 *C* and *D*). A short exposure to H_2 gas causes electron filling of preexisting hole states and leads to an increase in electrical resistance (Fig. 1*D*). On the other hand, O_3 exposure incorporates excess oxygen ion defects. The change in electrical resistance of NiO device with H_2 stimulus is found to decrease gradually upon repeated exposure and is substantially enhanced after the introduction of O_3, identical to the habituation and sensitization learning behavior observed in

Significance

Neuromorphic computing requires emulation of animal learning in synthetic matter. Materials with highly tunable electronic structures and a dynamical response to environmental stimuli are particularly suited for this task. Here, we demonstrate universal learning characteristics such as habituation and sensitization in a prototypical quantum material, NiO. With stimuli such as oxygen, ozone, and light, the concentration of atomic defects can be modulated reversibly, resulting in changes to electrical conductivity that mimic nonassociative learning. The material behavior inspires new algorithms for unsupervised learning in neural networks and opens up new directions for use of Mott insulators in artificial intelligence.

Author contributions: Zhen Zhang, J.M.A., K.R., K.M.R., and S.R. designed research; Zhen Zhang, S. Mondal, S. Mandal, J.M.A., N.A.A., A.F., Zhan Zhang, H.Z., H.C., F.R., J.L.M., Q.W., Y.S., K.R., and K.M.R. performed research; S. Mandal and K.M.R. analyzed data; Zhen Zhang, K.M.R., and S.R. wrote the paper; Zhen Zhang synthesized the materials and performed X-ray photoelectron spectroscopy and X-ray diffraction (XRD) measurements; Zhen Zhang and S. Mondal performed the habituation and sensitization experiments using NiO devices; S. Mandal carried out first-principles electronic structure calculations; N.A.A. and A.F. conducted midinfrared nanoimaging; Zhen Zhang, Zhan Zhang, H.Z., H.C., and Y.S. conducted synchrotron XRD and in situ and ex situ X-ray absorption near-edge spectroscopy measurement near the Ni K edge of devices; F.R. and J.L.M. performed X-ray absorption spectroscopy measurement near the Ni L edge and O K edge of devices; Q.W. fabricated the Pt top electrode of devices; and Y.A. conducted midinfrared nanoimaging.

Reviewers: N.B., Cornell University; and S.M., Drexel University.

The authors declare no competing interest.

[1]Zhen Zhang, S. Mondal, S. Mandal, and J.M.A. contributed equally to this work.

[2]To whom correspondence may be addressed. Email: zhenn.zhang@outlook.com, rabe@physics.rutgers.edu, or shriram@purdue.edu.

This article contains supporting information online at https://www.pnas.org/lookup/suppl/doi:10.1073/pnas.2017239118/-/DCSupplemental.

Published September 16, 2021.

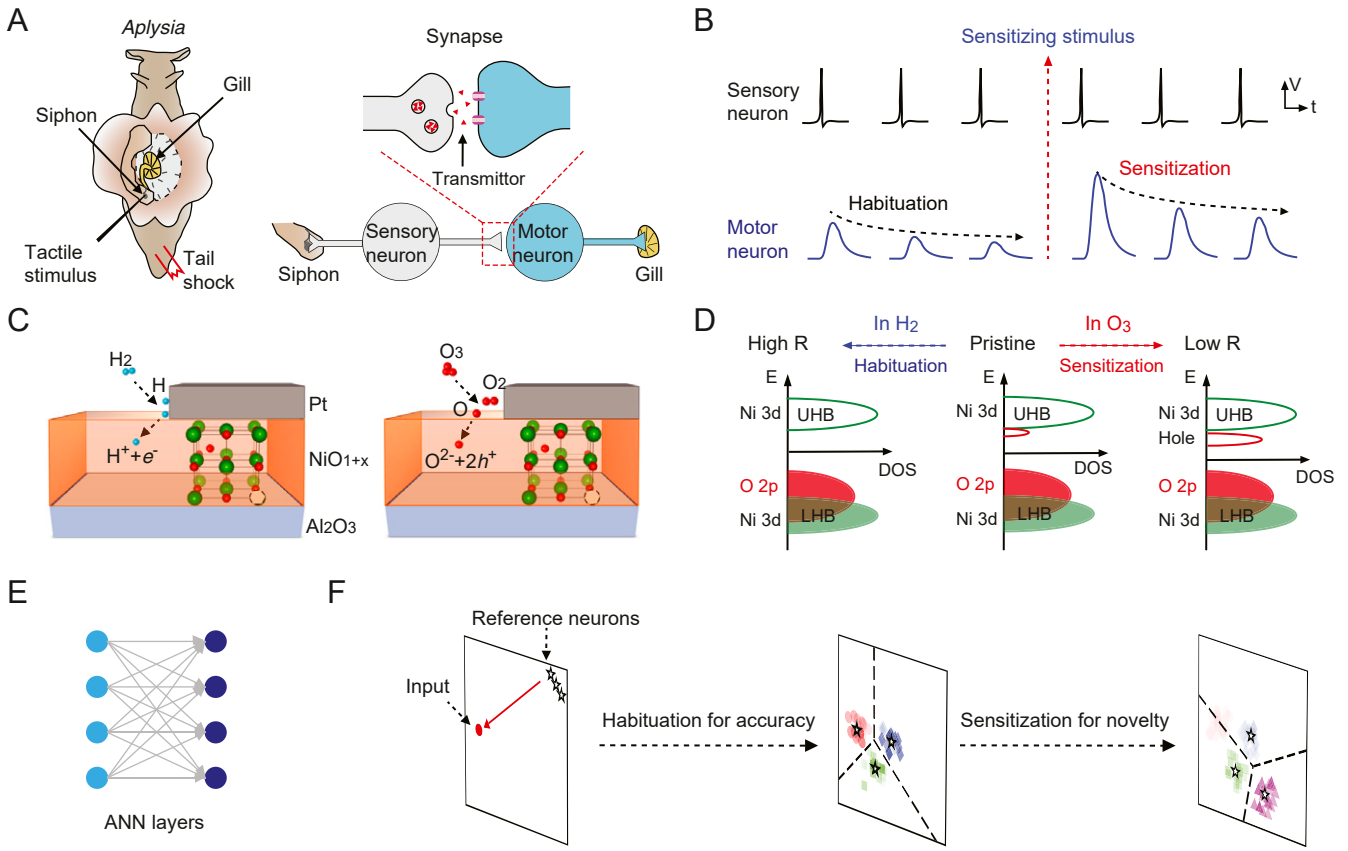

Fig. 1. Schematic illustration of nonassociative learning behavior including habituation and sensitization in *Aplysia* versus NiO devices. (*A*) Gill withdrawal reflex behavior of *Aplysia* and schematic of its neuron circuit. A light touch on the siphon leads the gill to withdraw. Repeating the tactile stimulus results in habituation learning behavior with reduced gill withdrawal. By applying a noxious stimulus, such as shock to the tail, the tactile induced gill withdrawal can be enhanced as a sensitization behavior (8). (*B*) The actional potential measured from the sensory neuron and motor neuron during the light tactile and sensitizing stimulus, where habituation is associated with the gradual diminishing of motor neuron potentials while sensitization is coupled with substantial enhancement of motor action potentials (11). (*C*) Schematic of habituation and sensitizing learning behavior in NiO devices. (*D*) A short exposure of the NiO device to H_2 gas causes electron filling and corresponding sharp electrical resistance increase. This response will gradually decrease, i.e., habituation, upon repeating H_2 exposure and being sensitized by exposure to an O_3 stimulus, which enriches the density of holes. (*E*) Example of a layer of synaptic connections in an ANN. (*F*) Unsupervised clustering task in a layer of an ANN employing habituation and sensitization inspired plasticity for improving accuracy and adaptability (*SI Appendix, Supplementary Note 2*).

Aplysia (Fig. 1*B*). Combined experimental and theoretical studies indicate that the environmental stimuli (gas or light) creates defects in the system and drives the material into metastable states dynamically, which is attributed to the observed electronic plasticity. Finally, we examine how such habituation and sensitization learning trends are beneficial in unsupervised clustering tasks, providing a more accurate solution with the ability to retain essential information under unexpected input variations (Fig. 1 *E* and *F*).

Results and Discussion

Habituation and Sensitization Behavior of NiO. Fig. 2 shows the experimental habituation and sensitization response of NiO devices under 5% H_2 exposure cycles and introduction of a short period of exposure to O_3. Initial response with 15 min of H_2 exposure and a relatively long time of H_2 withdrawal (15 min; Fig. 2*A*) demonstrate a reversible behavior and complete forgetting of previous cyclic exposures due to the long time interval in training serving as control studies. Reducing H_2 OFF time to 45 s while maintaining an identical H_2 ON time of 15 min (Fig. 2*B*), the response of NiO decreases monotonically, indicating habituation learning of the H_2 stimulus. When a short exposure to O_3 for 15 s was introduced in between the habituation training cycles (Fig. 2*B*), a substantially increased response appeared. The O_3 not only causes dishabituation but also results in an increase of response by ~10 times higher than that of pristine state, which is similar to the sensitization behavior observed in *Aplysia*. The resistance relaxation behavior during gas exposure and subsequently in the OFF state is modeled by a two-exponential function as $\frac{R}{R_0}(t) = \left(\frac{R}{R_0}(t=0) - A_1 - A_2\right) + A_1 \exp\left(-\frac{t}{\tau_1}\right) + A_2 \exp\left(-\frac{t}{\tau_2}\right)$, where τ_1 and τ_2 depict, respectively, the fast relaxation process which could be associated with defect exchange kinetics near the electrode–film interface region and the slower relaxation kinetics due to subsequent diffusion across the film thickness (19). It can be observed in Fig. 2*C* and *SI Appendix*, Fig. S2 that while the fast relaxation process τ_1 stays at a similar value (the catalytic activity of the electrode region does not change during the various exposures) the relaxation time τ_2 corresponding to the overall material behavior decreases clearly upon habituation and substantially increases with sensitization.

Additional training tests show that the habituation behavior of NiO devices is not a result of sample degradation (*SI Appendix*, Fig. S3). Moreover, habituation behavior is clearly seen with further reducing the H_2 OFF time scale (Fig. 2*D* and *SI Appendix*, Fig. S4), indicating a time-dependent plasticity of the learning feature of NiO. On the other hand, the magnitude of

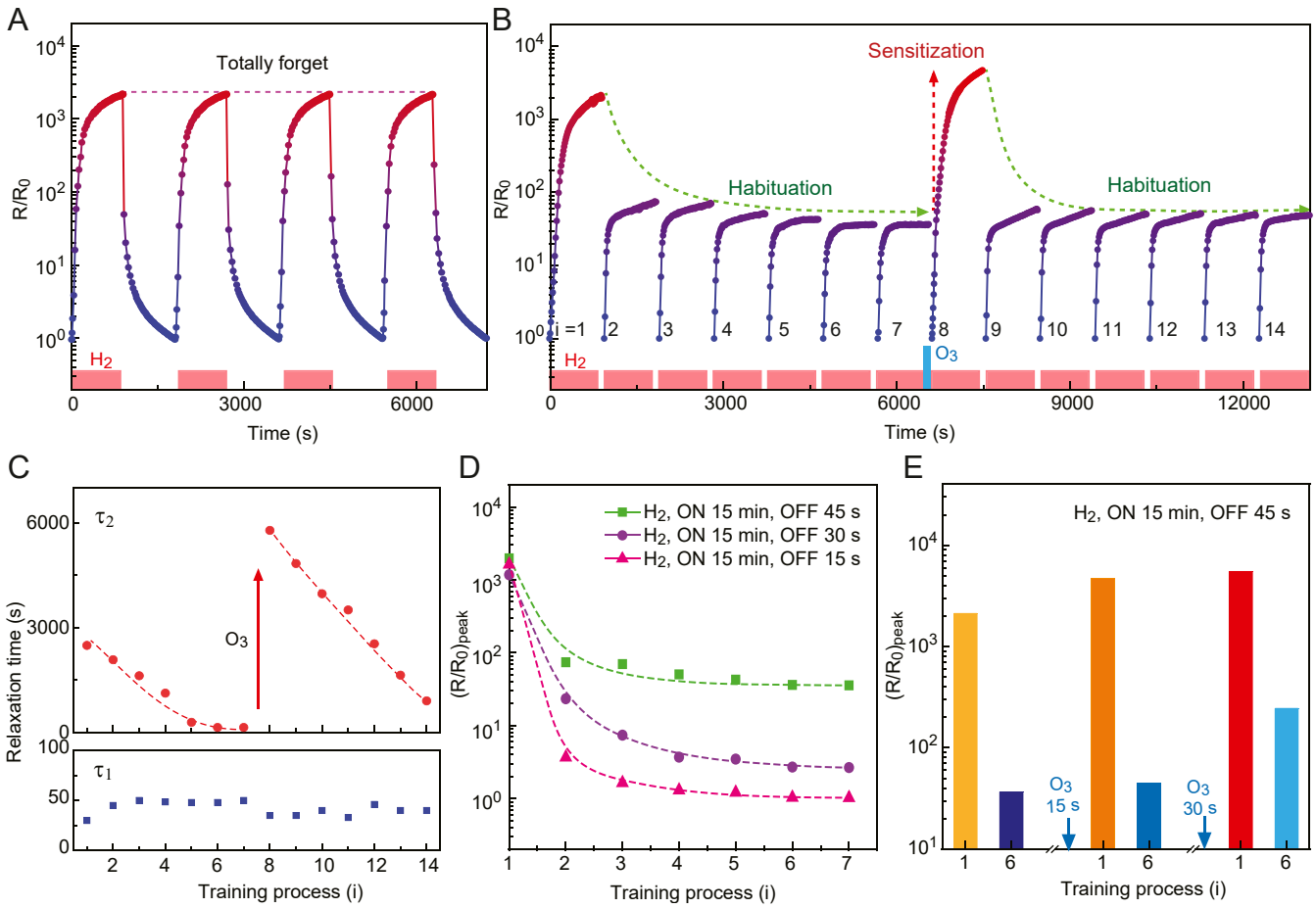

Fig. 2. Habituation and sensitization behavior of NiO devices under successive cycles of environmental stimulus. (*A*) Relative resistance change R/R_0 of NiO device under switching ON (15 min) and OFF (15 min) 5% H_2 for four exposure cycles at 200 °C. A reversible and nearly identical response is observed. (*B*) Response (R/R_0) of NiO devices under repeating expose to H_2 with an additional O_3 exposure before the eighth H_2 cycle. R_0 is the resistance of the devices at the beginning of each H_2 exposures. The H_2 OFF period is reduced to 45 s here. The O_3 exposure time is 15 s. With reducing the H_2 OFF time here, the response of NiO from the first to seventh H_2 exposures shows a continuous decrease, demonstrating a habituation learning behavior. After the O_3 stimulus, the response of NiO devices becomes even larger than that of first H_2 exposure, demonstrating a sensitization behavior. (*C*) Relaxation time as a function of the training process shown in *B*, where τ_1 and τ_2 were obtained by fitting the resistance response with a two-exponential function. (*D*) Time-scale dependence of habituation behavior of NiO devices. With shorter H_2 OFF time, the habituation behavior becomes more prominent, indicating a time-dependent plasticity. (*E*) Dependence of sensitization behavior on the strength of the O_3 stimulus. The response of NiO devices at first and sixth H_2 exposure becomes stronger with increasing the exposure time of the sensitization stimulus.

sensitization and the memory can be enlarged further by increasing the strength of sensitizing stimulus (i.e., the duration of O_3 exposure; Fig. 2*E* and *SI Appendix*, Fig. S5). Learning behavior can also be demonstrated by utilizing ultraviolet (UV) light at room temperature (*SI Appendix*, Fig. S6), suggesting general routes for the modification of electronic plasticity.

Mechanism Underlying the Evolution of NiO under Various Environmental Stimuli. Fig. 3*A* shows that the NiO is stable in air at 200 °C before introducing the gas stimulus. Upon introducing 5% H_2 gas, the resistivity increases gradually by approximately four orders of magnitude, while the resistivity of the sample drops by approximately two orders of magnitude during O_3 exposure, which indicates the metastability of NiO in H_2 and O_3 environment during the sensitization and habituation processes. To understand such environmental adaptation, we then quenched the metastable H_2- and O_3-exposed NiO devices to room temperature for further studies. Fig. 3*B* shows that the normalized second harmonic near-field amplitude plot of NiO with respect to Pt reference [s_2(NiO)/s_2(Pt)] is lower in H_2 than the pristine sample but higher when exposed to O_3 gas, indicating a microscopic modulation of carrier concentration in NiO under environmental stimuli (*SI Appendix*, Fig. S7). The structure evolution after the gas exposures was studied using X-ray diffraction (XRD) and shown in Fig. 3*C*. We observe a systematic shift of the NiO (111) diffraction peak, while the wide-range 2θ scan does not show any new diffraction peaks (*SI Appendix*, Fig. S8), which indicates that the NiO maintains the rocksalt structure with changing of defect states during gas exposures. The overall out-of-plane lattice change is ~0.27%, calculated based on the evolution of peak positions.

X-ray photoemission spectra were utilized to study the evolution of the defect state of NiO after gas exposures. The O 1s photoemission spectra of NiO are shown in Fig. 3*D* and fitted with photoemission from lattice oxygen with peak energy at ~529.3 eV (O_L, orange), oxygen defects (O_D, purple, peak energy at ~530.7 eV), and hydroxide group with peak energy located at ~531.7 eV (-OH, blue). Under H_2 gas, a predominance of the -OH group peak appears, indicating mainly the incorporation of hydrogen into the lattice from the Pt triple phase boundary (20). For O_3-exposed NiO (Fig. 3*D*), an enlargement of the defect oxygen peak (O_D) occurs, indicating the introduction of excess oxygen ions. Such an evolution of defect states in NiO is further confirmed with the Ni 2p photoemission shown in *SI Appendix*, Fig. S9 *A* and *B*. Taking the area ratio of lattice oxygen and oxygen defects, the composition of NiO in pristine and after O_3 exposure

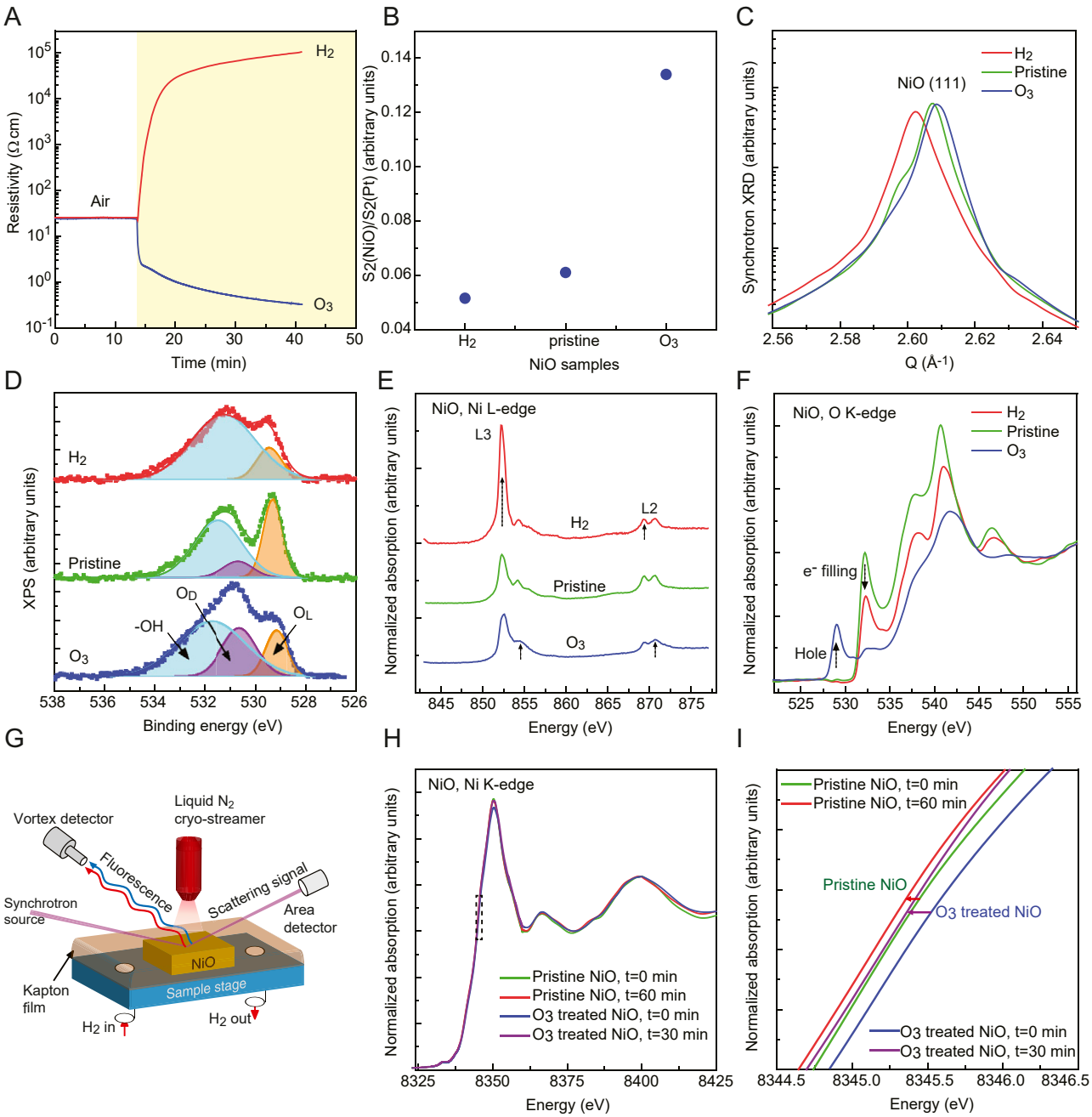

Fig. 3. Evolution of NiO upon H_2 and O_3 gas exposures. (*A*) In situ resistivity-time results of NiO devices during exposure of 5% H_2 and O_3 gases at 200 °C. (*B*) Normalized second harmonic near-field amplitude s_2(NiO)/s_2(Pt) of NiO devices, indicating an elevation of carrier concentration with H_2, pristine, and O_3 exposure, respectively. (*C*) Room-temperature synchrotron XRD profile of the NiO (111) peak after the exposures. Overall, the out-of-plane lattice constant of NiO changes by 0.27% between H_2 and O_3 exposures. (*D*) O 1s X-ray photoemission spectra of NiO after exposures, which were fitted with lattice oxygen of NiO (O_L, orange), excessive oxygen defects (O_D, purple), and hydroxide group (-OH, blue). A predominant hydroxide group peak in H_2-exposed NiO indicates the incorporation of hydrogen into the lattice, while the enlarged oxygen defects peak in O_3 exposed NiO demonstrate accumulation of excessive oxygen defects. (*E*) Normalized Ni L edge XANES spectrum of NiO after exposures. Under H_2 exposure, the spectrum weight shifts to lower energy level, indicating a decrease of the Ni valence state. On the contrary, after exposure to O_3, the spectral weight transfers to a higher-energy component, indicating an increase of the Ni valence state. (*F*) O K edge XANES spectra of NiO after exposures. In O_3, the prepeak at the O–K edge shifts its weight from ~532 eV to ~529 eV, indicating the formation of the hole state, corresponding to resistivity decrease. In H_2, the diminishing of the prepeak at ~532 eV indicates electron filling that results in substantial resistivity increase. (*G*) Schematic of the in situ XANES setup to monitor the response of NiO in H_2. (*H*) In situ Ni K edge XANES spectra of pristine and O_3-exposed NiO, where the marked area near the absorption edge is magnified in *I*. The lower energy shift of the absorption edge of O_3-exposed NiO (~0.2 eV) is larger than that of pristine NiO (~0.1 eV) after a shorter exposure period, confirming the sensitization behavior.

are estimated approximately to be $NiO_{1.19}$ and $NiO_{1.38}$, respectively (*SI Appendix*, Fig. S9*C*).

To understand the electrical response under gas exposures, we further study the Ni L as well as O K X-ray absorption spectra of NiO. Both Ni L-2 and L-3 absorption peaks show two components, i.e., ~870 eV vs. ~871 eV for Ni L-2 and ~853 eV vs. ~854 eV for Ni L-3. After exposure to H_2 gas, the spectral weight of the lower-energy component at both Ni L-2 and L-3 peaks

(Fig. 3*E*) increases substantially. At the same time, a diminishing of the prepeak at ~532 eV is observed at the O–K edge (Fig. 3*F*). This indicates electron filling of Ni 3d–O 2p hybridized orbitals upon hydrogenation, which compensates the preexisting hole state and leads to the increased NiO electrical resistance in H_2. Upon the sensitizing stimulus O_3 the spectral weight transfers to the higher-energy components at Ni L-2 and L-3 peaks (Fig. 3*E*). Notably, a new prepeak at the O–K edge emerges at ~529 eV at the expense of the one near ~532 eV (Fig. 3*F*), which indicates an increase in density of hole states and explains the decrease of electrical resistance of NiO in O_3 gas (Fig. 3*A*). Analysis of the Ni L-3 edge further confirms the corresponding variation at the valence state of Ni under gas exposures (*SI Appendix*, Fig. S10).

The sensitization behavior was further characterized using in situ X-ray absorption near-edge spectroscopy (XANES) measurement (Fig. 3 *G*–*I*). Both pristine and O_3-exposed NiO were sealed in an in situ environmental cell and heated up to 150 °C. The XANES spectra at the Ni K edge of NiO were continuously collected when H_2 gas was introduced. As shown in Fig. 3 *H* and *I*, the shifting of the Ni K absorption edge of O_3-exposed NiO is much larger than that of the pristine sample.

First-Principles Characterization of NiO with Excess Oxygen. We studied the incorporation of excess O atoms into NiO by putting one oxygen atom into randomly generated locations in a $2 \times 2 \times 2$ NiO supercell and optimizing the structures using density functional theory with a Hubbard U (DFT+U), which correctly gives an insulating antiferromagnetic ground state for pristine NiO (more details in *DFT+U Calculations*). We find two possible locations for an O atom, which are shown in Fig. 4 *A* and *B*. The energetically favorable location is the one where the excess O makes a weak peroxo-type bond with an O atom in the rocksalt structure, making a NiO_3 trimer (Fig. 4*A*). The bond length is 1.39 Å, which is longer than the interatomic distance 1.208 Å in molecular O_2. The computed formation energy relative to free atomic O is −0.39 eV. This is consistent with earlier studies on oxygen self-diffusion of NiO (21–23) in which defect states with excess oxygen as interstitial defect have been noted. In the second location, the excess O bonds with an Ni atom, similar to other Ni–O pairs (Fig. 4*B*). This configuration is ~4.5 eV higher in energy due to the difference in the nature of bonding of the added O to the rocksalt structure. The effects of the excess O on the electronic structures are quite different in the two locations. In location 1, the weak peroxo-type bond made by the added O to one of the oxygens in the rocksalt structure does not otherwise disrupt the electronic states of the pristine NiO. On the other hand, in location 2 two electrons are transferred from the added O to Ni, which results in significant changes to the hybridized Ni–O orbitals. Though much higher in energy, this bonding configuration is metastable because a transition to the lower-energy state would require an energetically costly rearrangement of the electrons and bonds as well as a symmetry breaking. This is consistent with the observed creation of holes in our experiment, and we speculate that the oxygen can be captured into this location adjacent to the Ni as it moves into the crystal. Next, we plot the total density of states (DOS) for the majority spin component for these two configurations and compare it with undoped NiO (Fig. 4 *C* and *D*). For the metastable configuration (Fig. 4*B*), the DOS shows a significant reduction of the bandgap, while for the energetically stable configuration with excess O the reduction of the bandgap appears to be very small.

For further investigation of the electronic-structure change due to excess oxygen atoms, we plot the projected DOS on various Ni atoms and the excess O atom in the supercell for the majority spin component. Generally, the first valence peak, which is known as the Zhang–Rice state for binary transition metal oxides, mostly consists of a strong hybridization between Ni-*3d* and O-*2p* orbitals and the first unoccupied peak in the DOS consists of mostly Ni-*3d* (*SI Appendix*, Fig. S11) (24). For the stable low-energy configuration (location 1), the excess O peaks mostly appear as the first valence band, which can otherwise strengthen the Zhang–Rice state in NiO (Fig. 4*E*). The first unoccupied Ni-*3d* peak splits into two, which is due to breaking of the symmetry of Ni atoms in the crystal. For the metastable configuration with excess O configuration (location 2), we see a dramatic change of the electronic structure. Here, we notice the appearance of new unoccupied states inside the gap between lower and upper Hubbard band, indicating their low electrical resistivity,

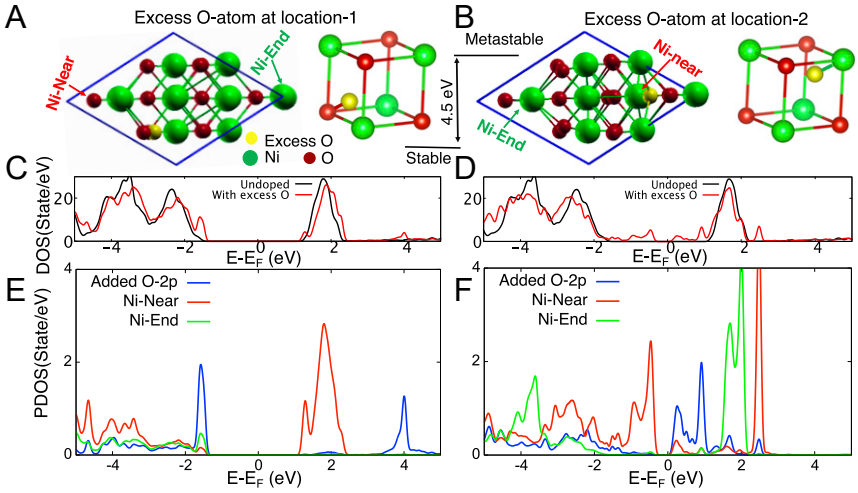

Fig. 4. DFT+U computed electronic structural change in NiO with the environmental stimulus of excess oxygen. (*A* and *B*) NiO with excess O (shown in yellow) atoms can potentially locate in two energetically favorable positions, one being stable and another in the metastable configuration. We denote them as location 1 and location 2 and present them in schematic diagrams; we label various Ni positions as Ni-Near and Ni-End. On the right we present the zoom-in view of added O in two different locations of rock-salt NiO. (*C* and *D*) The total DOS for the majority spin component with and without excess O in NiO. (*E* and *F*) Projected DOS for Ni-*3d* and O-*2p* for the excess O are plotted for these two configurations. For the stable configuration, the excess O appears as the top valence band while for more interesting metastable configuration it appears as the first unoccupied band, which is located inside the gap between lower and upper Hubbard band for undoped NiO.

consistent with the experimental observed electrical resistance modulation of NiO in O_3. The first unoccupied band in such a configuration is mostly O-*2p* (Fig. 4*F*), which is coincident with our experimental O K-edge X-ray absorption spectroscopy (XAS) spectra in Fig. 3*F*, where an additional absorption peak in the gap appears due to the excess O_3 environment. Thus, the metastable configuration studied theoretically could be similar to what we observe in the experiment where the removal of the O_3 environment reverts the system back to the original state. The dramatic decrease in resistivity with excess O in the experiment can be related to the metastable state of the excess O configuration, where the system undergoes a rearrangement of electronic states with an additional source of holes residing close to the Fermi energy.

Potential Neuromorphic Computing Application. Machine learning with artificial neural networks (ANNs) has dramatically expanded the scope of tasks that we can perform computationally. However, logically simulating these networks with traditional von Neumann architectures on CMOS (complementary metal–oxide–semiconductor) implementations consumes a tremendous amount of energy. An important goal in the field of neuromorphic computing is to improve the energy efficiency of these computations by implementing these networks in hardware, exploring beyond-CMOS devices that can mimic useful learning behaviors with analog computations. In this regard, the observed environmental learning behaviors in NiO presented above (Fig. 2*B*) are especially interesting as a starting point.

For example, these habituation and sensitization learning trends can be advantageously applied to online unsupervised learning algorithms on dynamic datasets (*SI Appendix*, *Supplementary Note 2*). When samples from differing input distributions are presented to a layer of competing reference vector neurons in an ANN, unsupervised Hebbian learning rules can perform an unsupervised clustering task to classify the data. However, such learning algorithms are traditionally susceptible to catastrophic forgetting when the different distributions are presented sequentially rather than interleaved. In such scenarios, a combination of habituation and sensitization behaviors, similar to those observed in NiO, can beneficially allow for local plasticity modulation—with habituation providing increased stability and sensitization enabling successful adaptation to novelty. In *SI Appendix*, *Supplementary Note 2* and Figs. S13 and S14and Movies S1–S8 we provide example simulations that demonstrate these benefits, resulting in a more accurate solution with the ability to retain essential information under unexpected input variations.

Conclusions

In conclusion, we have demonstrated nonassociative learning behavior in an inorganic system of binary nickel oxide under different environmental stimuli. Electronic plasticity is maintained by driving the system out of equilibrium and modulating defect concentration in dynamic environments. Inspired by the material response, neural networks incorporating habituation and sensitization can demonstrate superior clustering tasks. The results motivate new directions for strongly correlated insulators in emerging fields of artificial intelligence. Beyond NiO, other correlated materials which possess electronic structures sensitive to environmental perturbations and structural tolerance to defect exchange could be promising to further emulate diverse biological learning behavior.

Experimental Methods

Synthesis of NiO. NiO thin films with a thickness of ∼100 nm were deposited on *c*-plane sapphire substrates by the physical vapor deposition method. The substrates were cleaned with acetone and isopropanol and blow-dried with N_2 gas before being transferred into the growth chamber. Pure Ni target was magnetron-sputtered at a power of 100 W (direct current) under the pressure of 7 mtorr with flowing of a 10 sccm O_2 and 50 sccm Ar gas mixture. During the deposition, the temperature of the growth chamber was kept at 550 °C. The growth rate was ∼3 nm/min calibrated by X-ray reflectivity measurements. The NiO thin film was found to be epitaxially grown on substrate as (111) NiO // (0006) Al_2O_3 in the out-of-plane direction, and [$2\bar{1}\bar{1}$] NiO // [$11\bar{2}0$] Al_2O_3 in plane (*SI Appendix*, Fig. S1 *C* and *D*). Parallel platinum electrodes with a thickness of 100 nm were deposited on top of NiO thin films using shadow mask by electron beam evaporation. The width of Pt bars is 1 mm with spacing between them of 1.5 mm. Ohmic contact behavior was observed.

In Situ Electrical Measurements. Time-dependent electrical resistance measurements of NiO devices were conducted by continuously monitoring the voltage–current curves by sweeping a voltage from −0.1 V to 0.1 V with a step of 50 mV using a Keithley 2635A source meter. The device was connected to the measurement system with an insulating shielded cable to avoid environmental noises.

Environmental Chamber Setup. A testing chamber with switchable environments was utilized to study the response of NiO in a variety of stimuli. A schematic illustration of the chamber is shown in *SI Appendix*, Fig. S1*A*. A sealed temperature-controlled probe station was built to monitor the electrical properties of NiO thin films during changing the gas environment of the chamber. Extreme reducing and oxidizing environments with $p(O_2)$ spanning more than 30 orders of magnitude were generated by 5% argon-balanced H_2 gas [$p(O_2) \sim 10^{-30}$ atm] and O_3 gas [effective $p(O_2) \sim 10^5$ atm, *SI Appendix*, *Supplementary Note 1*]. We monitored the oxygen partial pressure of 5% H_2 by a zirconia-based oxygen sensor and estimated the effective $p(O_2)$ of ozone based on the thermal equilibrium between O_3 and O_2 following literature reports. The gas flow was kept as 100 mL/min to enable a steep switch of chamber environment (*SI Appendix*, Fig. S1*B*). During use the environmental chamber was located in a fume hood for safety.

Habituation and Sensitization Test Procedure.

Habituation in repeating H_2 ON/OFF cycles. We explored the habituation behavior of NiO devices by periodic exposure of hydrogen (5% of H_2) gas in the environmental chamber. The measurement was performed at a constant temperature of 200 °C. Before the habituation and sensitization test, the pristine devices were isothermal at 200 °C for 1 h in air to obtain a stabilized defect state. The response of devices was monitored by switching ON and OFF 5% H_2 for many cycles. The H_2 ON time was maintained as 15 min for the devices to reach a metastable high-resistance state. The H_2 OFF time was selected spanning from 15 min, which shows totally forgetting behavior to 15 s with substantial habituation learning behavior. The time-dependent plasticity on habituation behavior was further studied by varying H_2 OFF time as 15 s, 30 s, and 45 s.

Sensitization by exposure to O_3. In this work, multiple strong stimuli were introduced to explore the sensitization behavior of NiO devices. Exposure to O_3 gas in a short period of time with a flow rate of 100 mL/min by using an ozone generator was found to trigger the sensitization behavior. To study the dependence of sensitization on O_3 strength, the duration of O_3 exposure was varied from 15 s to 30 s. To characterize the sensitization behavior, the response of the device to repeating H_2 exposure was monitored.

Room-temperature realization of habituation and sensitization. The habituation and sensitization were further investigated at room temperature using UV light as a sensitization stimulus. During the habituation experiment, an exposure of 5% H_2 (15 min) to the device was performed alternatively in an interval of withdrawal H_2 for 15 min. At room temperature, such a narrow interval is insufficient to remove hydrogen from the device. As a result, the device shows a weak H_2 habituation. Exposure to UV light was utilized to sensitizing device response to repeating H_2 exposure at room temperature. The UV light source from BHK Inc. was used with an output wavelength spectrum from λ = 185 to 579 nm, an output power of 7,500 Vrms, and a current of 30 mA. The operating frequency of UV light is 50 Hz. The devices were exposed to the UV light for 5 min from a distance of 3 cm. The UV light breaks the environmental O_2 to form O_3, which sensitizes the devices.

XRD Measurements. Synchrotron XRD measurements were carried out on a Newport Kappa diffractometer at beamline 33-ID at the Advanced Photon Source. X-ray energy of 8,333 eV, which is below the Ni absorption edge (∼8,345 eV), was selected. The diffraction signals in the vicinity of sapphire (0006) and NiO (111) Bragg peaks were measured with a PilatusII-100K detector. Additional XRD measurements over a wide angle were conducted at ambient conditions using the Panalytical MRD X'Pert Pro diffractometer under Cu $K\alpha$ radiation. For XRD measurements, NiO devices were exposed in

H_2 and O_3 gas for 30 min at 200 °C and subsequently quenched to room temperature while maintaining the H_2 and O_3 gas flow.

Ni L Edge and O K Edge XAS Measurement. The absorption spectroscopy on the O K edge and Ni L edge of NiO thin films was performed at beamline 29-ID IEX at the Advanced Photon Source, Argonne National Laboratory. Data were collected in total fluorescence yield in a pressure better than 1×10^{-8} Torr using a multichannel plate located at $2\theta = 20°$ with 7° angular acceptance. Circular polarized X-ray with an overall energy resolution better than 100 meV was used. The incidence angle was $\theta = 5°$, which was set to limit the penetration depth to 10 nm and 40 nm at the O K and Ni L edges, respectively. Using the drain current from a gold mesh upstream of the sample, the total fluorescence yield was normalized by the incident X-ray intensity. For this measurement, the samples were exposed to 5% H_2 and O_3 gas at 200 °C for 30 min.

In Situ Ni K Edge XANES Measurement in H_2. The XANES measurements were carried out at beamline 33-ID at the Advanced Photon Source. The fluorescence signal from the sample was measured with a Vortex detector. The X-ray energy was scanned through the Ni K edge between 8,310 and 8,560 eV. The incident angle was selected as 5° to preferentially probe Ni valence states throughout the film. The NiO devices were mounted in a thin film cell (25) at the center of a six-circle diffractometer (Fig. 3*G*). An Oxford Instrument liquid N_2 cryostreamer was used to elevate the sample temperature up to 150 °C. A 3% H_2 balanced by helium gas was flowed through the sample cell during the measurements. For in situ XANES measurements, pristine and O_3-exposed NiO devices were utilized to compare the evolution of the Ni K edge in an H_2 gas environment. The O_3 exposure on NiO was conducted at 200 °C for 10 min.

X-Ray Photoemission Measurement. X-ray photoelectron analysis of NiO thin film after exposing in 5% H_2 and O_3 gas was performed using a Kratos X-ray photoemission spectrometer with Al $K\alpha$ radiations (1,486.6 eV). The binding energy was calibrated by a C1s XPS peak located at 284.6 eV. For this measurement, the devices were exposed at 200 °C for 30 min and quenched to room temperature in 5% H_2 and O_3 gas.

Midinfrared Nanoimaging. We used scattering-type scanning near-field optical microscopy (s-SNOM) to carry out the experiments. A platinum-coated tip oscillating at 280 kHz frequency is illuminated by a quantum cascade laser beam at $\lambda = 10.5$ μm at angle of 45° to the sample surface. The backscattered light is demodulated at higher-order harmonics of tip resonance frequency and detected using phase modulation (pseudoheterodyne) interferometry. s-SNOM functions as a local probe of material properties at high spatial resolution (~20 nm), providing simultaneous topography and near-field midinfrared images of sample, allowing mapping of dielectric property variations (26). For the measurement, the NiO devices were exposed to 5% H_2 and O_3 gas at 200 °C for 30 min and quenched to room temperature.

DFT+U Calculations. We performed DFT-based computations within the generalized gradient approximation of Perdew–Burke–Ernzerhof for exchange and correlation (27) using ultrasoft pseudopotentials as implemented in the QUANTUM ESPRESSO software (28). In our DFT+U computation, we used $U = 7.0$ eV (29). The plane wave kinetic energy cutoff was set to 100 Ry with a corresponding charge density cutoff of 400 Ry. The lattice parameter of NiO (4.171 Å) is obtained from the experiment. We consider antiferromagnetic ordering along [111] (AFM II), which leads to R3m space group symmetry, in a $2 \times 2 \times 2$ supercell with 32 atoms. We further tested our results for $3 \times 3 \times 3$ supercell with 108 atoms (*SI Appendix*, Fig. S12).

Data Availability. All study data are included in the article and/or supporting information.

ACKNOWLEDGMENTS. This research used resources of the Advanced Photon Source, a US Department of Energy (DOE) Office of Science User Facility operated for the DOE Office of Science by Argonne National Laboratory under contract DE-AC02-06CH11357. Additional support was provided by NSF grant DMR-0703406. This work was supported in part by Center for Brain-inspired Computing, a Joint University Microelectronics Program center sponsored by the Semiconductor Research Corporation and Defense Advanced Research Projects Agency, and by the NSF, Intel Corporation, Sandia National Labs, and the Vannevar Bush Fellowship. We acknowledge Air Force Office of Scientific Research grants FA9559-16-1-0172 and FA9550-18-1-0250, Army Research Office grant W911NF1920237, Office of Naval Research grant N00014-17-1-2770, and NSF grant 1904097 for support. S.M. and K.M.R. acknowledge the computational support by the Frontera supercomputer, NSF OAC-1818253, at the Texas Advanced Computing Center at The University of Texas at Austin. Zhen Zhang thanks C. Huang, X. Chen, and T. J. Park for assistance with device fabrication.

1. G. W. Burr *et al*., Neuromorphic computing using non-volatile memory. *Adv. Phys.* **2**, 89–124 (2017).
2. D. A. Pomerleau, Efficient training of artificial neural networks for autonomous navigation. *Neural Comput.* **3**, 88–97 (1991).
3. P. M. Attia *et al*., Closed-loop optimization of fast-charging protocols for batteries with machine learning. *Nature* **578**, 397–402 (2020).
4. J. M. Stokes *et al*., A deep learning approach to antibiotic discovery. *Cell* **180**, 688–702.e13 (2020).
5. E. R. Kandel *et al*., *Principles of Neural Science* (McGraw-Hill, New York, 2000).
6. T. J. Carew, C. L. Sahley, Invertebrate learning and memory: From behavior to molecules. *Annu. Rev. Neurosci.* **9**, 435–487 (1986).
7. S. Ginsburg, E. Jablonka, Epigenetic learning in non-neural organisms. *J. Biosci.* **34**, 633–646 (2009).
8. E. R. Kandel, The molecular biology of memory storage: A dialogue between genes and synapses. *Science* **294**, 1030–1038 (2001).
9. T. Carew, V. F. Castellucci, E. R. Kandel, Sensitization in Aplysia: Restoration of transmission in synapses inactivated by long-term habituation. *Science* **205**, 417–419 (1979).
10. H. M. Pinsker, W. A. Hening, T. J. Carew, E. R. Kandel, Long-term sensitization of a defensive withdrawal reflex in Aplysia. *Science* **182**, 1039–1042 (1973).
11. V. Castellucci, E. R. Kandel, Presynaptic facilitation as a mechanism for behavioral sensitization in Aplysia. *Science* **194**, 1176–1178 (1976).
12. F. Zuo *et al*., Habituation based synaptic plasticity and organismic learning in a quantum perovskite. *Nat. Commun.* **8**, 240 (2017).
13. J. Zaanen, G. A. Sawatzky, J. W. Allen, Band gaps and electronic structure of transition-metal compounds. *Phys. Rev. Lett.* **55**, 418–421 (1985).
14. N. Tsuda, K. Nasu, A. Fujimori, K. Siratori, *Electronic Conduction in Oxides* (Springer Science & Business Media, 2013).
15. A. G. Gavriliuk, I. A. Trojan, V. V. Struzhkin, Insulator-metal transition in highly compressed NiO. *Phys. Rev. Lett.* **109**, 086402 (2012).
16. S. G. Hu *et al*., Emulating the Ebbinghaus forgetting curve of the human brain with a NiO-based memristor. *Appl. Phys. Lett.* **103**, 133701 (2013).
17. Q. Wang, A. Puntambekar, V. Chakrapani, Vacancy-induced semiconductor-insulator-metal transitions in nonstoichiometric nickel and tungsten oxides. *Nano Lett.* **16**, 7067–7077 (2016).
18. G. H. Aydogdu, D. Ruzmetov, S. Ramanathan, Metastable oxygen incorporation into thin film NiO by low temperature active oxidation: Influence on hole conduction. *J. Appl. Phys.* **108**, 113702 (2010).
19. L. Chen, C. L. Chen, A. J. Jacobson, Electrical conductivity relaxation studies of oxygen transport in epitaxial $YBa_2Cu_3O_{7-\delta}$ thin films. *IEEE Trans. Appl. Supercond.* **13**, 2882–2885 (2003).
20. I. Hotovy *et al*., Enhancement of H_2 sensing properties of NiO-based thin films with a Pt surface modification. *Sens. Actuators B Chem.* **103**, 300–311 (2004).
21. C. Dubois, C. Monty, J. Philibert, Oxygen self-diffusion in NiO single crystals. *Philos. Mag. A Phys. Condens. Matter Defects Mech. Prop.* **46**, 419–433 (1982).
22. M. O'Keeffe, W. J. Moore, Diffusion of oxygen in single crystals of nickel oxide. *J. Phys. Chem.* **65**, 1438–1439 (1961).
23. C. Dubois, C. Monty, J. Philibert, Influence of oxygen pressure on oxygen self-diffusion in NiO. *Solid State Ion.* **12**, 75–78 (1984).
24. S. Mandal, K. Haule, K. M. Rabe, D. Vanderbilt, Influence of magnetic ordering on the spectral properties of binary transition metal oxides. *Phys. Rev. B* **100**, 245109 (2019).
25. H. Zhou *et al*., Understanding controls on interfacial wetting at epitaxial graphene: Experiment and theory. *Phys. Rev. B Condens. Matter Mater. Phys.* **85**, 35406 (2012).
26. Y. Abate *et al*., Nanoscopy of phase separation in $In_xGa_{1-x}N$ alloys. *ACS Appl. Mater. Interfaces* **8**, 23160–23166 (2016).
27. J. P. Perdew, K. Burke, M. Ernzerhof, Generalized gradient approximation made simple. *Phys. Rev. Lett.* **77**, 3865–3868 (1996).
28. P. Giannozzi *et al*., QUANTUM ESPRESSO: A modular and open-source software project for quantum simulations of materials. *J. Phys. Condens. Matter* **21**, 395502 (2009).
29. F. Tran, P. Blaha, K. Schwarz, P. Novák, Hybrid exchange-correlation energy functionals for strongly correlated electrons: Applications to transition-metal monoxides. *Phys. Rev. B Condens. Matter Mater. Phys.* **74**, 155108 (2006).